
# On the behavior of rainfall maxima at the eastern Andes

R. Hierro, Y. Burgos Fonseca, M. Ramezani Ziarani, P. Llamedo, T. Schmidt, A. de la Torre, P. Alexander

PII: S0169-8095(19)31023-3

DOI: https://doi.org/10.1016/j.atmosres.2019.104792

Reference: ATMOS 104792

To appear in: *Atmospheric Research*

Received date: 6 August 2019

Revised date: 13 November 2019

Accepted date: 21 November 2019

Please cite this article as: R. Hierro, Y. Burgos Fonseca, M. Ramezani Ziarani, et al., On the behavior of rainfall maxima at the eastern Andes, *Atmospheric Research*(2018), https://doi.org/10.1016/j.atmosres.2019.104792

# On the behavior of rainfall maxima at the eastern Andes

Hierro R.[a], Burgos Fonseca, Y.[d], Ramezani Ziarani, M.[b,c], Llamedo, P.[a], Schmidt, T.[c], de la Torre, A.[a], Alexander, P.[d]

a CONICET / Facultad de Ingeniería, Universidad Austral, LIDTUA (CIC), Argentina

b University of Potsdam, Institute of Geosciences, Potsdam, Germany

c Helmholtz Centre Potsdam, GFZ German Research Centre for Geosciences, Potsdam, Germany

d CONICET / Instituto de Física de Buenos Aires (IFIBA), Buenos Aires, Argentina

Corresponding author: rhierro@austral.edu.ar

Abstract

In this study, we detect high percentile rainfall events in the eastern central Andes, based on Tropical Rainfall Measuring Mission (TRMM) with a spatial resolution of 0.25x0.25°, a temporal resolution of 3 hours, and for the duration from 2001-2018.. We identify three areas with high mean accumulated rainfall and analyze their atmospheric behaviour and rainfall characteristics with specific focus on extreme events. Extreme events are defined by events above the 95th percentile of their daily mean accumulated rainfall. . Austral summer (DJF) is the period of the year presenting the most frequent extreme events over these three regions. Daily statistics show that the spatial maxima, as well as their associated extreme events, are produced during the night. For the considered period, ERA-Interim reanalysis data, provided by the European Centre for Medium-Range Weather Forecasts (ECMWF) with 0.75° x0.75° spatial and 6 hourly temporal resolutions, were used for the analysis of the meso- and synoptic-scale atmospheric patterns. Night- and day-time differences indicate a nocturnal overload of northerly and northeasterly low-level humidity flows arriving from tropical South America. Under these conditions, cooling descending air from the mountains may find unstable air at the surface, giving place to the development of strong local convection. Another possible mechanism is presented here: a forced ascent of the low-level flow due to the mountains, disrupting the atmospheric stratification and generating vertical displacement of air trajectories. A Principal Component Analysis (PCA) in T-mode is applied to day- and night-time data during the maximum and extreme events. The results show strong correlation areas over each subregion under study during night-time, whereas during day-time no defined patterns are found. This confirms the observed nocturnal behavior of rainfall within these three hotspots.

## 1. Introduction

Rainfall distribution and occurrence over South America (SA) are strongly determined by their low-level circulation and by the presence of the Andes range. Moist air coming from the Atlantic Ocean enters the continent at northern Brazil and continues its journey westward over the Amazon basin (e.g. Fernandez et al. 2006, Gulizia et al. 2013). It finally reaches the eastern Andes and heads towards the south (Seluchi and Marengo, 2000). This is the South Atlantic subtropical high, which transports moist air from the

ocean to the Amazon basin and toward extratropical South America (Vera et al., 2006a). The south-north flow at the western side of the Andes suggests that polar air masses are introduced by the Pacific subtropical high, giving place to a high contrast in the meridional component of the wind along the eastern side of the range, from higher to lower latitudes. This behaviour is also observable in humidity, yielding a good correspondence between moist air and meridional wind. A regional reinforcement of this southerward flow at the east of the Andes generates the principal low-level transport mechanism of the continent, the South American Low-Level Jet (e.g. Virji 1981; Paegle et al. 1987). Regarding rainfall itself, Hoffmann (1975) identified the north-south aligned precipitation band at the east of the Andes, reaching 30ºS latitude with maximum at approximately 23ºS over the mountains. As shown by Vera et al. (2006b), by September the convection migrates from Central America into SA, starting the wet season over the equatorial Amazon and spreading fast to the southeastern side of the region. Abundant rainfall follows the onset over the Amazon basin and lasts for about one month (e.g., Kousky 1988; Horel et al. 1989; Marengo et al. 2001; Liebmann and Marengo 2001). This, in turn, is followed by a more frequent northerly cross-equatorial flow (Marengo et al. 2001; Wang and Fu 2002). Seasonal changes of convection in tropical SA may be explained by the changing moisture content of the planetary boundary layer as well as by temperature changes at its top (Vera et al., 2006b and references therein). Romatschke and Houze (2013) stated that solar heating triggers convection of small horizontal dimensions over the slopes of the Andes. Moist flow coming from the Atlantic is capped by dry westerlies at the lee side of the range, making the diurnal lifting over the mountains one of the main factors for convection development (de la Torre et al., 2004; Rasmussen and Houze 2011). Saavedra et al (2019) have tested the output of precipitation in several high spatiotemporal simulations over the Peruvian area using different topography and land use data sources. A clear influence of moisture flux and its convergence in the Andes-Amazon transition was found, with differences of up to 25% in precipitation due to orography or land use changes. Kumar et al. (2019) identified precipitating cloud systems in order to investigate the influence of surface wind flow and topography on precipitation over South America. They found that its features are modulated by different directional flows, giving place to higher rain rates at the eastern slope as compared to the western side and to brighter band characteristics in the northern vs. the southern Andes.

Montero-Lopez et al. (2014) pointed out that the understanding of the influence of tectonic forcing on climate and surface processes is closely linked to the knowledge of orographic development of mountain belts and its distribution. In addition, they argued that the south-central Andes region presents an asymmetric distribution of rainfall because high mountain range altitudes and meteorological precipitation mechanisms affect erosion and deposition.

Extreme rainfall is one of the major factors that control the hydrological cycle of SA, triggering landslides and flash floods along the eastern side of the Andes (e.g. Boers et al., 2015 and references therein). Marengo et al. (2012) showed that floods in the Amazon river are related to positive precipitation anomalies as well as to the time when extreme rainfall occurs. The direction of the low-level flow drives the occurrence of extreme events both along the Amazon basin and to the south, after it turns to the Peruvian and Bolivian Andes (Boers et al 2014). Bookhagen and Strecker (2008) explained this effect as a result of moist air lifting over the mountains along the eastern slope of the central Andes and determined that extreme events in the tropics are driven by the low-level flow. As stated by these authors, rainfall has a direct impact in shaping hillslope morphology and determining fluvial characteristics in mountain belts. In turn, mountain range relief and its relationship with orographic rainfall may result in different landscapes, where the mean precipitation in geological timescale is one of the key factors in the development of the Andes range (e.g. Lowman and Barros, 2014 and references therein).

Moreover, this precipitation may produce spatial correlations between fast tectonic uplift and strong rainfall, even in the absence of any erosional influence on tectonics (Whipple 2009). In the case of the Andes range, the extremely asymmetrical distribution of rainfall owing to the high topography strongly affects erosion and deposition. A key concept regarding the interactions between orography and climate interactions is based on the idea that, over a region with similar geologic conditions, wet climate produces slower erosion than under dry conditions (Bookhagen and Strecker (2012). Severe socio-economic effects are present along the Andes as a result of downstream floodings and landslides produced by strong precipitation events (e.g. Moreiras, 2005; Harden 2006). The aim of the present work is to locate and characterize extreme rainfall events at the east of the subtropical Andes. The evolution of their occurrence time is described and some statistical results that may be used to allow better forecasting of their presence over this region are included. In

section 2, we present the data used and describe the methodology employed. In section 3, we characterize the maximum and extreme events found, and in section 4 their dynamical conditions in different scales are considered. In section 5, a principal component analysis is performed, and in section 6 we outline some concluding remarks.

## 2. Methodology and database

We focus this study on the east of the Andes, in the region enclosed by [15S -27S, 70W-60E], where strong signals of mean accumulated rainfall have been systematically observed (e.g. Hierro et al., 2016) (Fig. 1). As mentioned by Rivera et al (2018) (and references therein), South America presents limitations in its rainfall network as regards the density and frequency of observations. Moreover, over complex orography areas, large uncertainties appear due to difficulties in accessing the rain gauges. Considering the high quality of TRMM verified data, the chosen period under analysis runs from summer 1998 to winter 2018. 3-hourly (0.25 x 0.25 km) accumulated rainfall data (*R*) are obtained from the Daily TRMM and Others Rainfall Estimate product (TRMM 3B42 V7 derived Data). The use of these data over any topographic region in South America offers a significant advantage, as far as this technique is not obstructed by orographic features. Technical details can be found in Kummerow et al. (2000), among others. TRMM data have been validated over different regions and seasons around the world. Huffman et al (2007) found that these data successfully reproduce the observed precipitatation at small scales and are able to detect large daily events. Habouchian et al. (2007) validated daily TRMM data over the subtropical Andes and found some limitations in these measurements associated with the type and location of the event in relation with the orography. Over the central Andes region, Mantas et al. (2015) found these products to be in good agreement with rain gauges during one-week periods, also detecting a strong dependence on the analysed region, characterized by clearly diverse orography and climate features. Extreme precipitation events in the range of 50–200 mm/day and areas affected by high rainfall amounts have been well determined by TRMM data over the Philippines (Jamandre and Narisma, 2013). From TRMM measurements, Fonseca and Cavalcanti (2012) detected a correlation between extreme precipitation, flooding and landslide events along the eastern South America coast. This was found to be a response to an excess of daily rainfall and to the synoptic system over that region.

Fig. 1a shows the daily accumulated field of $R$ ($R_d$) during the 1998-2018 period, averaged over the region involved in the study. After a convenient rescaling of a portion of this figure, three relative strong mean $R_d$ signals are observable over the base of the mountains, at the lee side of the Andes (Fig. 1b).

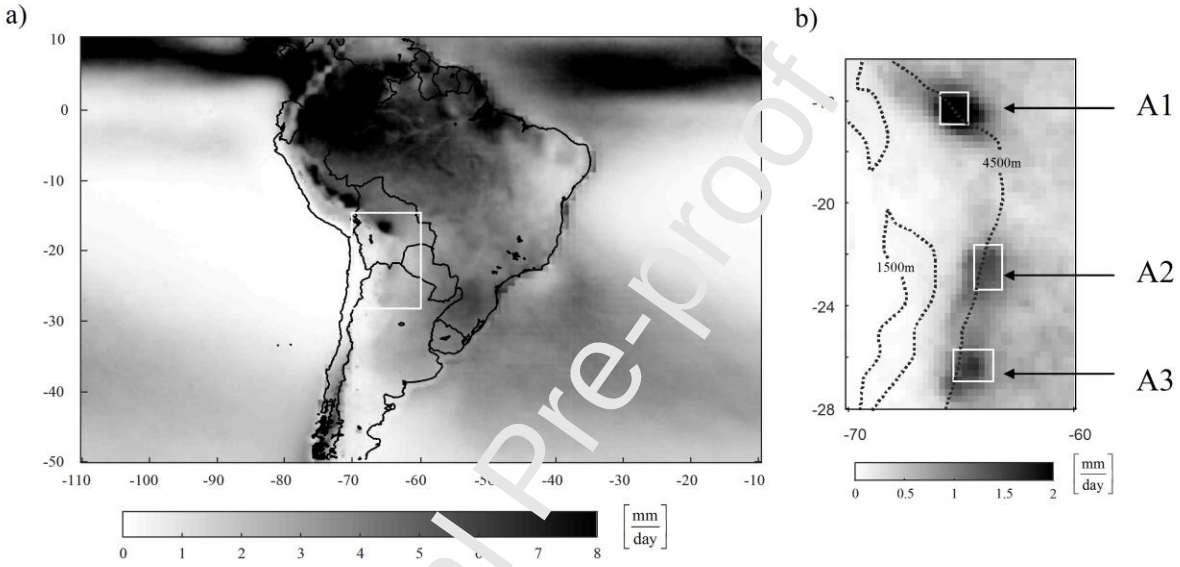


Fig. 1. a) Mean daily $R$ ($R_d$) during the period 1998-2018 over South America and b) the same variable over the selected region, showing the subregions under study, A1, A2 and A3, respectively. The white rectangle in a) is expanded in b), with the scale conveniently rescaled. Note that in b) $R_d$ values saturate above 2 mm/day.

Each one of these preeminent $R_d$ signals was arbitrarily enclosed into subregions A1 (16-17S, 64.5-65.5W), A2 (22-23.5S, 63.5-64.5W) and A3 (26-27S, 63-65W), respectively (Fig. 1b). This allows to quantify 3 sets of spatial maximum precipitation events, respectively over A1, A2 and A3 (hereinafter, called M1, M2 and M3). In doing so, the methodology applied to detect M1, M2 and M3 is based on a comparison of rainfall at each Ai with that observed in an extended region around it (see Appendix for details)). Following the establishment of M1, M2 and M3, the days detected within each subregion, now under the constraint imposed by the 95$^{th}$ percentile over M1, M2 and M3 (45mm/day, 28mm/day and 22mm/day), are called extreme event days. These are grouped in sets E1, E2 and E3, respectively.

## 3. Maximum and extreme values of precipitation

The dynamical condition characterizing these extreme cases is explored using Era-interim reanalysis with a spatial resolution of 0.75º. After identifying the hotspots and taking into account that previous studies have extensively discussed different initiation mechanisms for convection and moist instability regimes depending on local time, day- and night-time data are separately considered below. Day-time is defined as the interval 21Z-00Z before the event day, and night-time as the interval 00Z-09Z during the event day. Below, M(i)day / M(i)night and E(i)day / E(i)night) represent, respectively, Mi and Ei associated to day-time / night-time, where i = 1, 2, 3.The monthly distribution of maximum rainfall reveals that December to March (austral summer) are the months with highest occurrence (Fig 2a). $\overline{R}_{48hr}$ is defined by averaging all Mi events every 3 hours during the day of the event and the day before. It is computed over 3-hour intervals during M1, M2 and M3, and is shown in Fig. 2b, including the median, to test a possible influence of outliers on the data. Shaded areas in this figure indicate the event day. For M1, 06Z (3 a.m. or 2 a.m. local time (LT)) indicates the mean maximum rainfall. Remarkably, the rainfall increase begins during the previous hours, whereas its intensity decreases after the 06Z peak of the event day. In the cases contained in M2, the time of maximum precipitation occurs earlier, at 03Z. The total evolution resembles a one-wavelength structure, with maximum and minimum values respectively at 03Z and 12 hours later, at 15Z. M1, M2 and M3 indicate low values of $\overline{R}_{48hr}$ during the first 24 hours (the day preceding the maximum event), with a slight increase during the last hours and a steep increase at the beginning of the event day. This behavior clearly evidences the occurrence of a systematic nocturnal maximum of precipitation within each subregion.

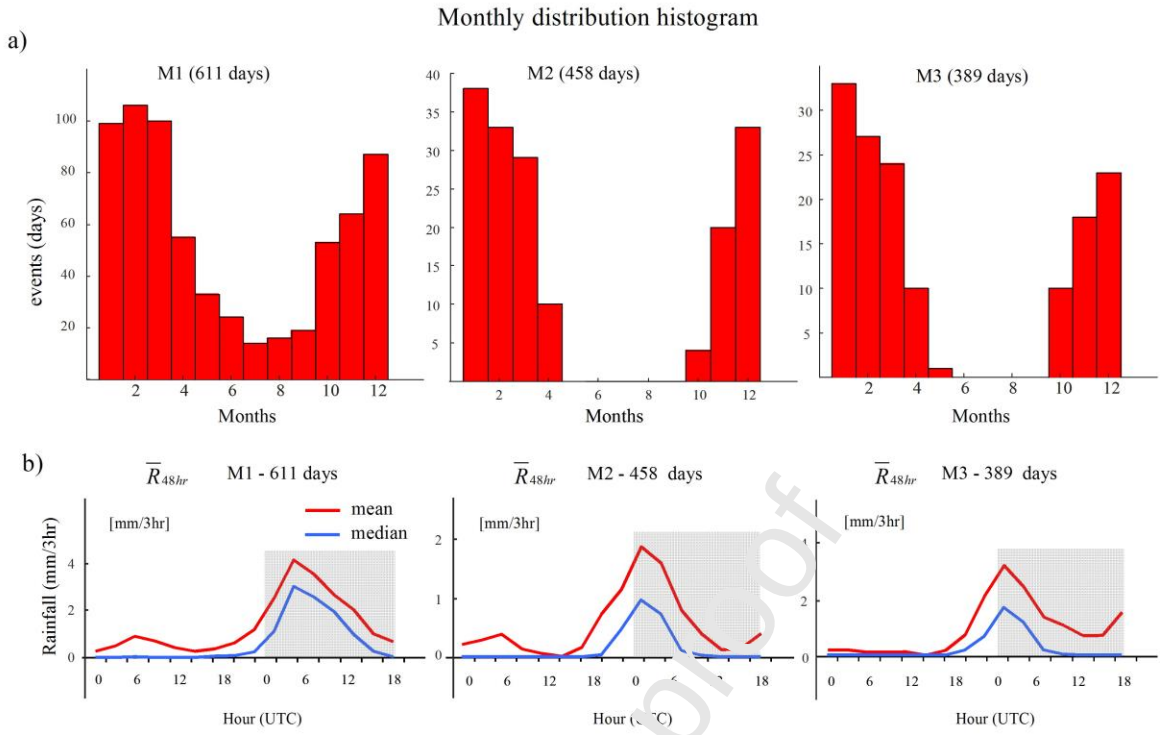


Fig. 2. a) Monthly distribution of M1, M2 and M3. b) Mean and median of *R* over each region during each event day and the previous day. Shaded areas indicate the event day. Local time (LT) corresponds to UTC-3 or UTC-4, depending on the region. Peaks occur at 2 a.m. or 3 a.m. (LT) in M1 cases, and 11 p.m. or 12 a.m. (LT) in M2 and M3 cases.

Following the definition given above, we select extreme events for each subregion. Figure 3a shows the monthly distribution of E1, E2 and 3.

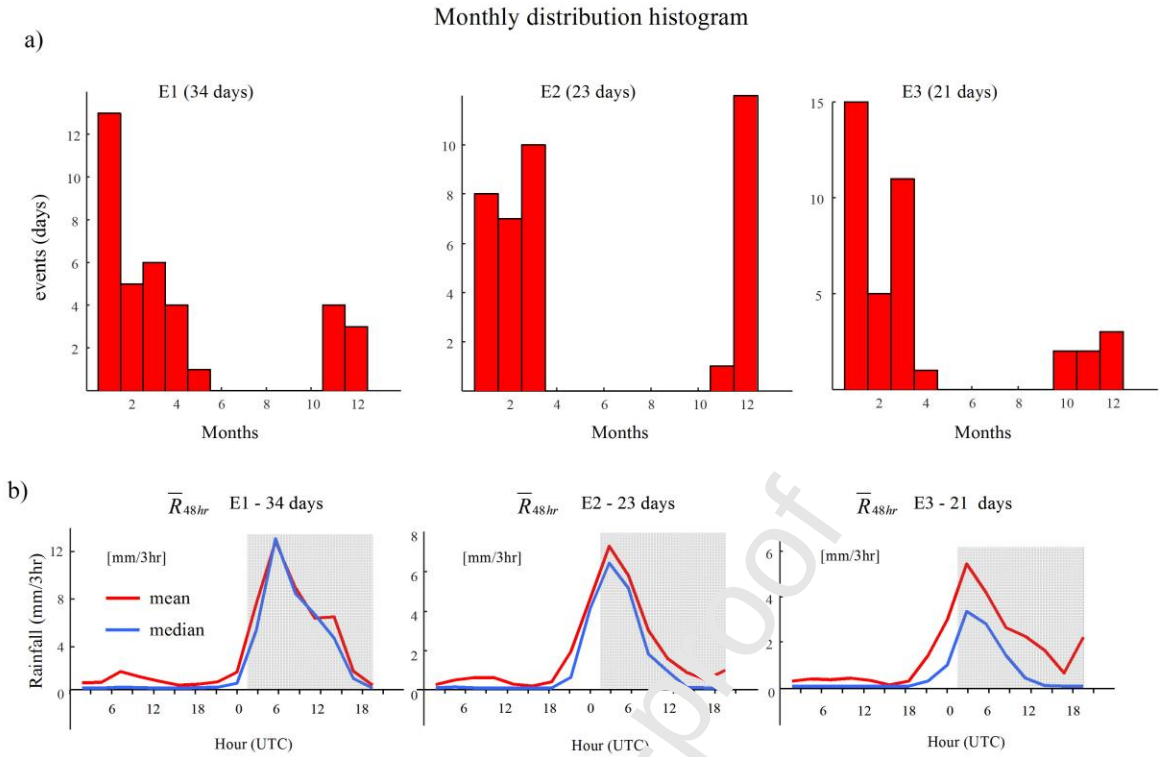


Fig. 3. Same as Fig. 2, now for E1, E2 and E3. Peaks occur at 2 a.m. or 3 a.m. (LT) in E1 cases and 11 p.m. or 12 a.m. (LT) in E2 and E3 cases.

In all cases, summertime includes more extreme events and wintertime remains empty of data in all cases. E1 shows January as the month with more frequent extreme events and in general, austral summer appears as the period with the highest activity. In E2 this is clearer, with almost all the events taking place between December and March. A similar behaviour is observed in E3, where January-March is the period with more frequent extreme events. Mean and median of $\overline{R}_{48h}$ (Fig. 3b) clearly show low values during the previous day, with a steep increase starting before 18Z. As observed in M1, M2 and M3, these extreme rainfalls originate during the previous day, mostly in the interval 18-21Z. Only E1 presents a steep slope beginning on 00Z of the extreme event day. This (shaded area) shows a behavior similar to that of M1, M2 and M3, with increasing values of rainfall during the local night, reaching a maximum at 06Z in E1 events and 03Z in the two others.

Previous works have already documented persisting mesoscale convective systems clouds at the region considered (e.g. Rozante and Cavalcanti, 2008). From numerical simulations and satellite imagery, this night rainfall behaviour has been already found close to this region (e.g. Tratche et al, 2010). A possible mechanism explaining this phenomenon can

be found, for example, in Chavez and Takahashi (2017) -and references therein-, who stated that, when cooling downslope air converges at the surface with low-level unstable layers, a precipitation maximum may occur at the base of the mountain. Banta, 1990 and references therein, established the presence of three ingredients: 1) a conditionally unstable temperature lapse rate, which is important mostly in the warm season, 2) an initiation or triggering mechanism provided daily by mountain circulations, and 3) adequate moisture, which is generally advected in by the larger-scale flow. We know that adiabatic lifting represents the most important process in the atmosphere, since air can be brought to saturation by evaporation, by cooling, or by expansion from adiabatic lifting. In effect, mountains produce rising motion and adiabatic ascent in two ways: forced ascent and convergence caused by the heating of elevated topography. Under the first mechanism, mountains disrupt atmospheric stratification and force vertical displacement of air trajectories. In these regions, moist air ascents and clouds can form. Then, in addition to the stability properties of the atmosphere, the characteristics of the flow disturbance caused by the lifting created by the mountain appear to be essential. A major difference between potential and latent instability (see Iribarne and Godson (1973)) is that mountain lifting does not affect the potential stability or instability of a layer with respect to its vertical displacement. However, it can destabilize a column of the atmosphere with respect to vertical parcel displacements in such a way that a stable column becomes unstable. Following this concept, the question is whether the flow pattern is able to lift air to its lifting condensation level and form clouds. Moreover, if the flow pattern is able to lift air at any level to its level of free convection, unstable cumuliform clouds can form; if not, the clouds will be stable or stratiform (Banta, 1990). An alternative point of view to explain the occurrence of nocturnal mountain rainfall was proposed by Barros and Lang (2003), who analyzed a nocturnal storm case close to the Himalaya range, detected using TRMM data. They found that a constant night and day flow is blocked by the mountains, giving place to convergence at low levels. This convergence is weakened during the day by upslope flow, which, in turn, reduces the spatial gradients in wind. At night, however, the convergence close to the surface increases due to decreasing wind intensity at lower levels, which yields upward motion and convection. This convection is intensified by the increase in advected moisture and by the nocturnal increasing instability caused by the interaction between the diurnal atmospheric cooling and heating and the steady enhancement of moisture close to the surface. The nocturnal peak is thus produced by the surface forcing, the instability coinciding with available humidity.

## 4. Large and small-scale dynamical conditions

Following the arguments in section 3, the dynamical differences affecting extreme events between day and night are distinguished using Era-interim reanalysis, under a spatial resolution of 0.75º. According to Figs. 2 and 3, the increasing values of rainfall during the night begin at approximately 18Z of the day before the event.

We test the specific humidity ($q$) and lower levels wind ($\vec{V}$) patterns during extreme days (Fig. 4) using Erainterim reanalysis each 3 hours. We define day-time as 18Z-21Z (subindex d) of the day before the event and night-time (subindex n), as 00Z-12Z of the event day. Fig. 4a-c shows the mean humidity transport at 850 hPa, calculated as $\vec{q_T} = q\vec{V}$. In all cases, a strong humidity transport from the North following the climatological low-level circulation is observed mainly during summer, when moist air from the Atlantic goes through the Amazon region. Then, it is channelled towards the south, giving place to the South American Low Level Jet (SALLJ) events. This transport undergoes a rotation close to latitudes defining each extreme events subregion, yielding to an accumulation of humidity at the base of the mountains.

Figures 4e-f present the differences between the average, for E1, E2 and E3, of $\vec{V}_{(d)}$ and $\vec{V}_{(n)}$, $\Delta\vec{V} = \vec{V}_{(n)} - \vec{V}_{(d)}$ (differential wind) at 850 hPa and the mean specific humidity at the same level ($\bar{q}$) (shaded). As mentioned before, this variable seems to reach higher values close to the base of the mountains at the lee side of the range over the studied area of each extreme, following the transport pattern shown in figures 4a-c. The differential wind shows a zonal westwards component during the night in each case. This gives place to a

convergence over the mountains, where a core of humidity prevails over the region. This behaviour is emphasized in Fig. 5, which shows the mean differential zonal wind averaged over each latitude band corresponding to E1, E2 and E3. As can be seen, the maximum negative values at the subregions immediately to the west of the mountains are more evident for E1 and E3 than for E2.

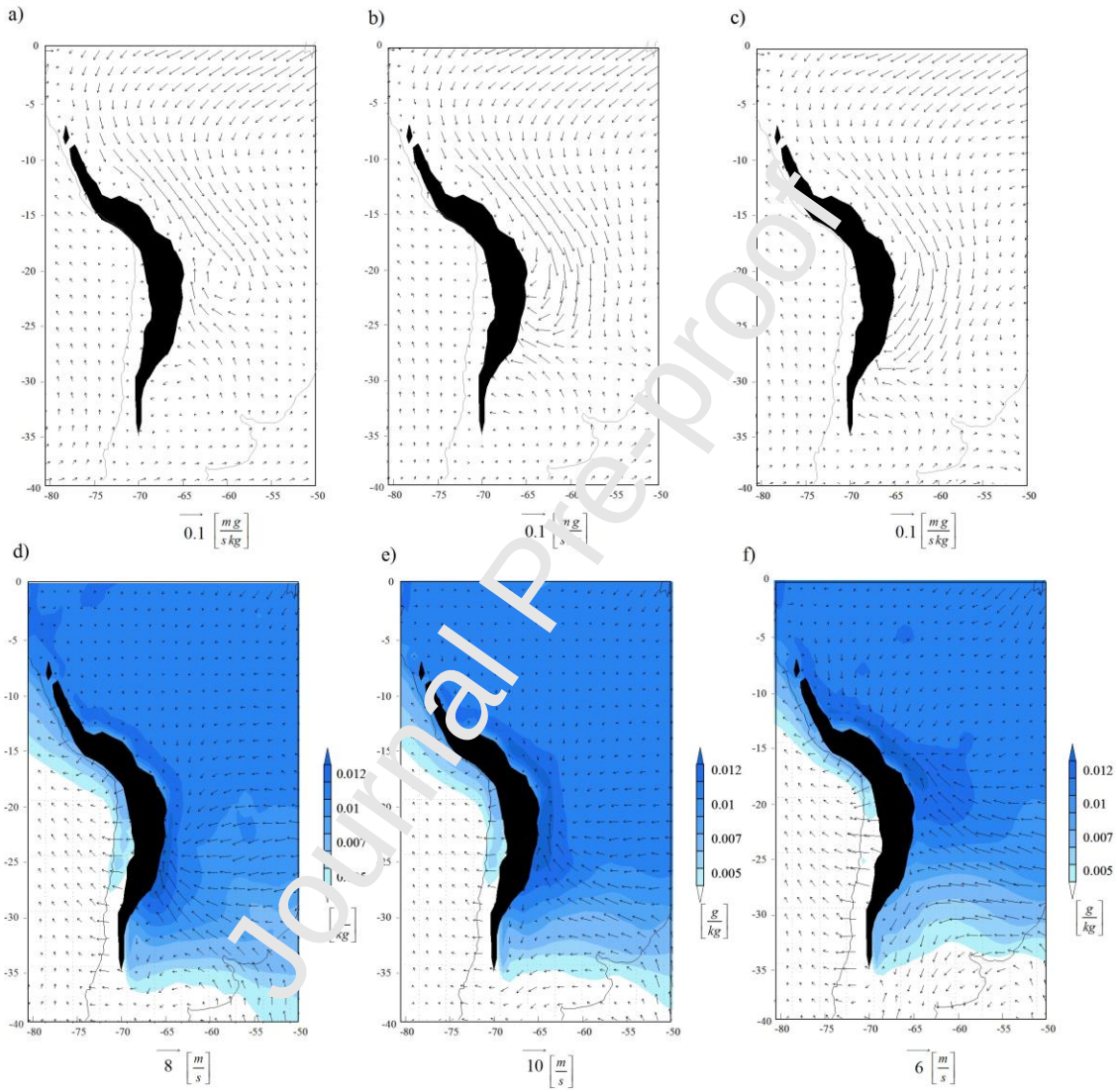


Fig. 4. a-c) Mean humidity transport (in m g / s kg) at 850 hPa for E1, E2 and E3, respectively. d-f) Differential wind (in m/s) (night-day) at 850 hPa averaged for E1, E2 and E3, respectively, and the mean specific humidity at the same level (shaded).

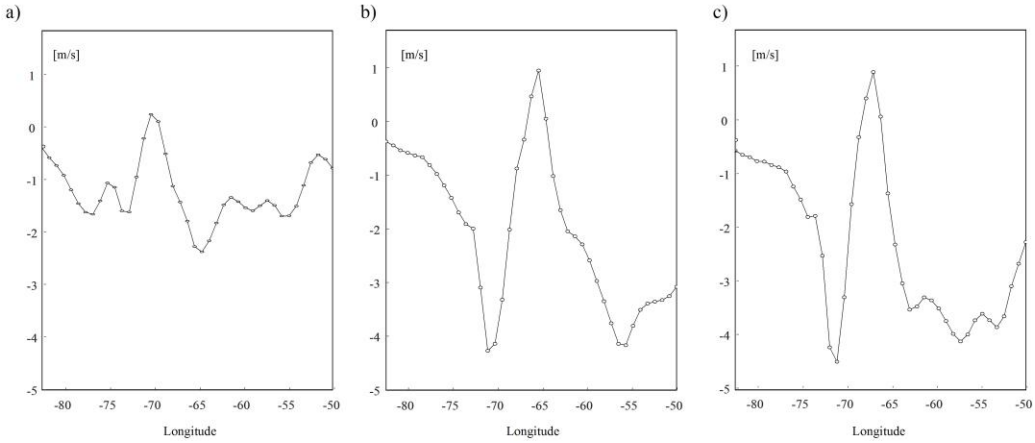


Fig. 5. Mean difference night - day of zonal wind averaged over each latitude band corresponding to E1, E2 and E3.

## 5. Principal Component Analysis

In previous meteorology and climatology studies some elementary features of events characterized by large data sets have been detected by applying Principal Component Analysis (PCA). In particular, some tropospheric and stratospheric mechanisms over South America were successfully analysed through this technique (e.g. Compagnucci et al., 2001a). There are six different recognized ways to interpret PCA: Q, R, P, O, S and T modes (Cattell, 1952). In this case, given the expected relevance of the spatial variability, the most useful mode to be applied is the T-mode (e. g. Compagnucci et al., 2008). In T-mode, the statistical variables are defined by the spatial fields of the studied variable at a given time. The grid points are the statistical observations and the domain is given by the time of occurrence. The obtained time series are called PC loading. They show the moment of occurrence of a given pattern, called PC scores, and also indicate their significance with respect to the actual field at that time. In T-mode, the PC loadings represent the correlation between the pattern represented by the PC scores and the actual field of the variable. The PC scores, in turn, provide the patterns which correspond to the leading spatial field. As stated by Compagnucci et al. (2001), T-mode determines the main spatial pattern field types in a parameter. In this work, a PCA analysis in T-mode is separately applied to M(i) and E(i) night and day respectively, over the region studied. This allows to determine the correlation areas of rainfall for each M(i) and E(i) during night and day with a certain percentage of explained variance. It is not referred to the PC

loadings, since we are not dealing with time but with selected cases, so we cannot consider the temporal behavior of the PC scores.

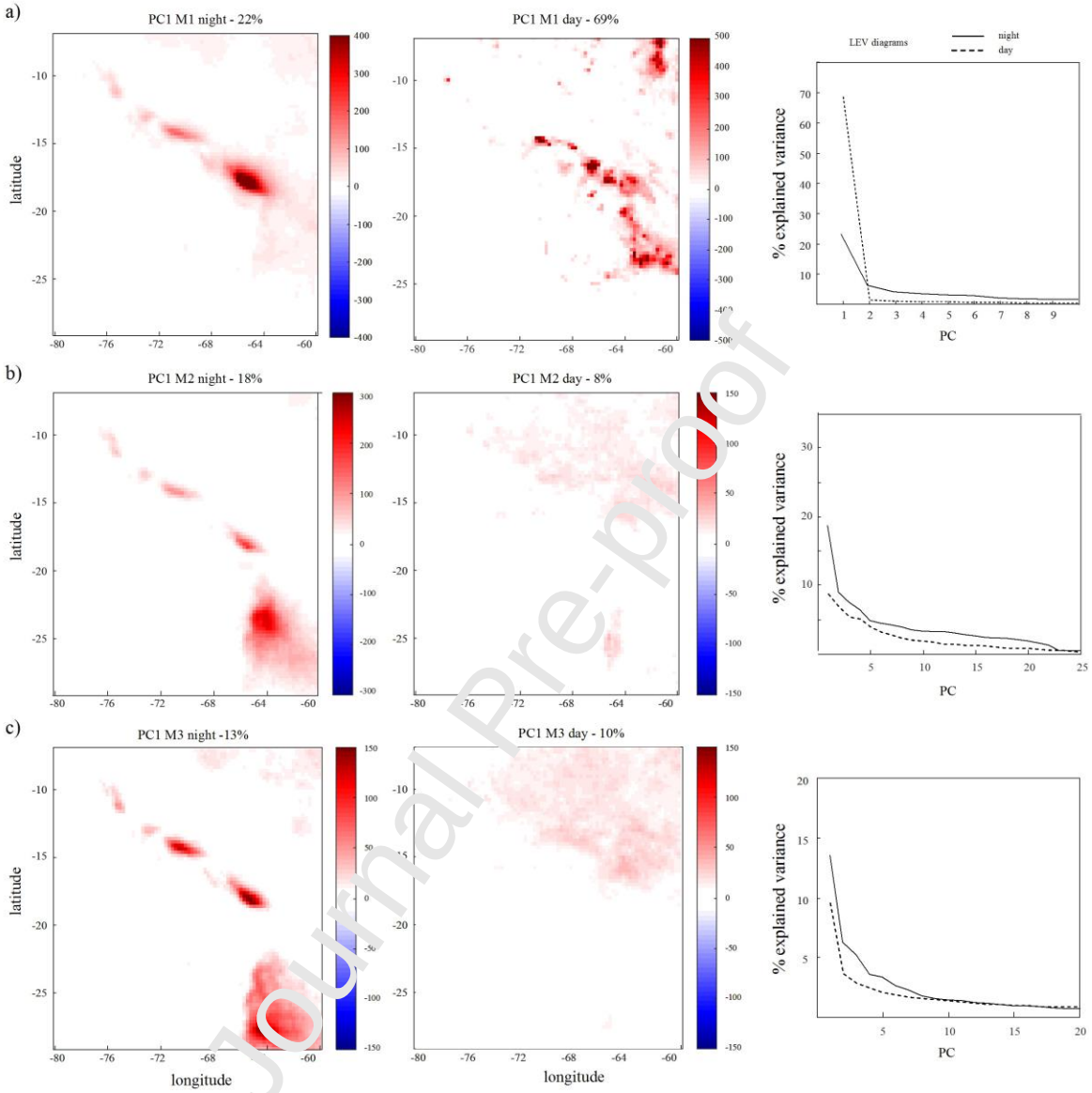


Fig 6. a-c) T-Mode applied to M1, M2 and M3 events. On the left side, PC1 at night-time is shown; on the center, PC1 at day-time; on the right side we present the explained variance for PC1 at night-time (solid line) and day-time (dashed line)

Fig. 6 presents PC1 in T-mode applied to M1, M2 and M3 during night-time and day-time, following the definitions given in section 2. It is important to mention that we do not show the PCs loadings. This is due to the fact that we are dealing with case studies, which are not equally spaced in time, so we cannot consider time series. However, we point out that

in all cases, they are positive, which means that the patterns shown in each PC1 are always the same. Fig. 6a, corresponding to M1, shows a strong positive correlation among grid points over A1 during the night, with an explained variance of 22%. During day-time (Fig 6a center), there are no clear correlated regions. Although it seems that there are some positively correlated areas close to A1, this PC explains around 70% of the total variance, with a small contribution of the other PCs (Fig 6a right). In the case of night-time, PC1 and PC2 contribute 22% and 5% respectively, while the rest present smaller values. Fig 6b (left) shows M2 PC1 during night-time. As in the previous case, we can distinguish the A2 grid points with a strong positive correlation, explaining around 18% of the total variance. On the right side, we can see that the second PC explains around 5% of the total variance, decreasing with increasing PCs. During day-time (Fig 6b center) it is clear that no correlation among points is found in PC1 scores. Although 8% seems to be a small value, it is the largest one compared with the other PCs. The following pattern (PC2) -not shown-, presents a similar behaviour without correlation in A2 and the others. Similar results are found for PC3 during the night (Fig 6c, left) and during day-time when there is no correlation over A3. Both cases present low values of explained variance; however, PC2 explains around 5% in each one, decreasing with the following PCs.

This procedure was also followed for E1, E2 and E3. Fig 7a (left) shows positive correlation over A1 during night to PC1. Around 44% of the variance is explained by this PC. PC1 during day-time does not show any correlation in the region. Although not shown, the following PCs do not show significative values. As in the case of M2, Fig 7b (right) presents PC1 scores with high positive values over A2 during night-time. In this case, this PC explains 46% of the total variance, whereas the second only explains around 10% (Fig 7b center). During day-time again, no correlation is found in PC1, and the following E3 cases, shown in Fig 7c (right), exhibit high correlation over A3, explaining 40% of the total variance during night-time. As with the remaining events, E3 during day-time does not show a clear pattern in PC1 scores.

From the PCA applied both to maximum and extreme events, we can see that the latter contain less dispersion than the former, since the total explained variances are always higher.

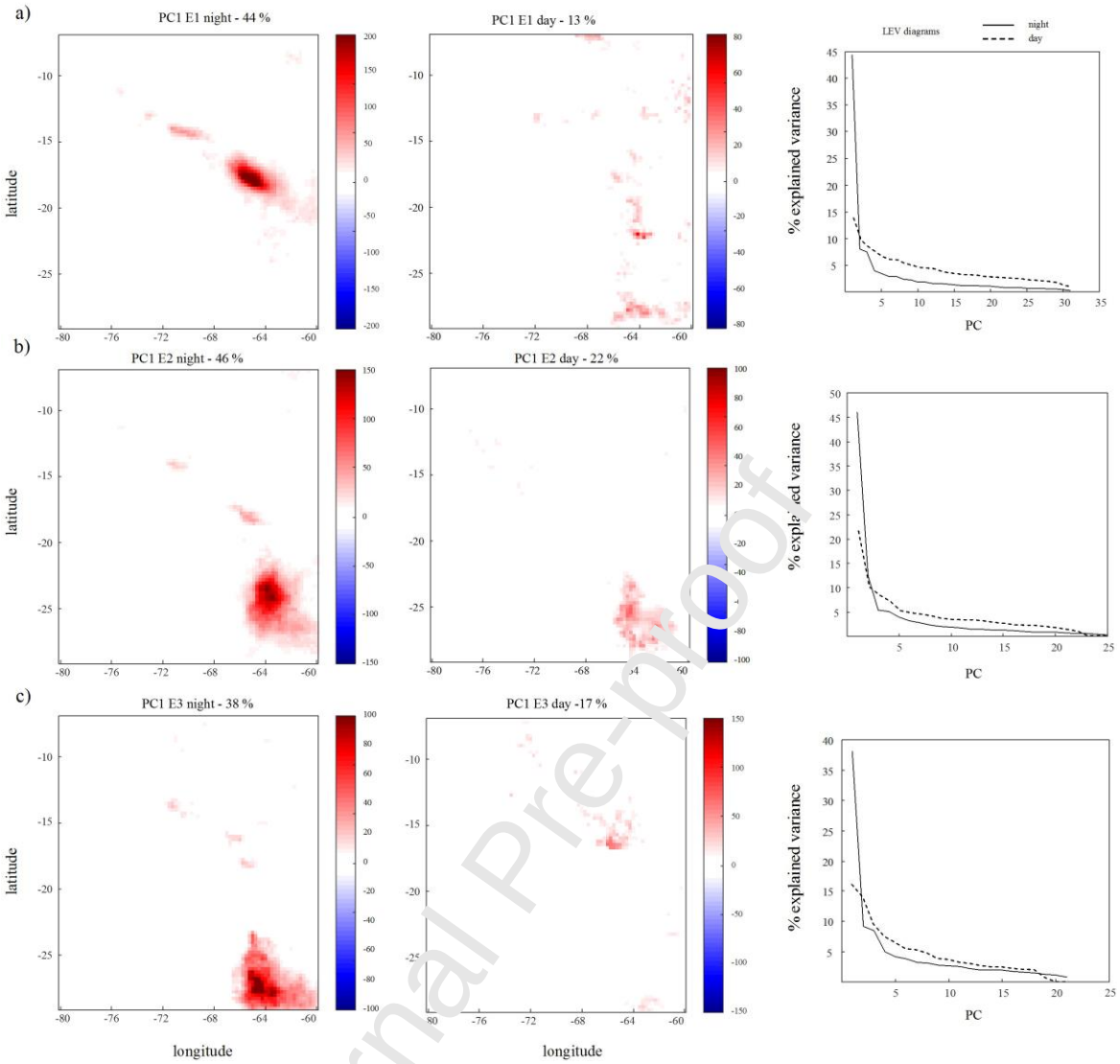


Figure 7. Idem Fig 6 for E1, E2 and E3.

## 6. Summary and conclusions

Looking at the mean field of daily accumulated precipitation over the study region, three regions with relative maximum values were identified. 611, 458 and 389 cases (days) respectively, were found. Austral summers are the periods with higher frequencies of occurrence. Night peaks were found in all cases. The 95th percentile of each one was considered as a cutoff for extreme events. The cutoff values were 45 mm/day, 28 mm/day and 22 mm/day for each region respectively. 34 days, 23 days and 21 days with extreme values were found in each region respectively. The monthly distribution of days with extreme values shows austral summer as the period of higher activity for each one.

January, and December-March and January-March are the periods where the occurrence of these extreme values is most frequent. Their daily average also shows peaks at night. The average daily evolution shows a similar behavior in the three cases, with increasing values of rainfall during the local night, reaching a maximum at 06Z. The idea of night convection given by cooling descending air that reaches unstable air at the base of the mountains was tested using Erainterim data. It shows that during the night, there is an increase of differential humidity over the regions studied. In all of them, we found stronger low-level winds and a differential northern transport of humidity with a strong meridional component during the night. Through PCA, it was determined that, for maximum events, there is a strong correlation among grid points over each area studied during the night time, defined as 00Z-09Z of the event day. The day-time events (18Z-21Z of the day after of the event), in turn, show that there is no correlation found at any PC. The same occurs for extreme events, which present less dispersion considering their enhanced variance explained by PC1 with respect to maximum events. We can conclude that in the presence of humidity and warm air mostly during the last hours of summer days, extreme precipitation may occur in the region under study during local night hours. Two mechanisms are proposed as possible sources of this rainfall distribution: i) cooling downslope air converging at the surface with low-level unstable layers and ii) a forced lifting created by the mountains.

*Acknowledgements*

The study has been supported by the CONICET under grants CONICET PIP 11220120100034 and ANPCYT PICT 2013-1097 and by the German Federal Ministry of Education and Research (BMBF) under grant 01DN14001 The TMPA data were provided by the NASA/Goddard Space Flight Center's Mesoscale Atmospheric Processes Laboratory and Precipitation Processing system.

**Appendix**

The methodology applied to detect the relative spatial maximum is as follows. First, the total mean of $R_d$ for the complete time interval (2001-2018) is computed. This is

performed within each Ai subregion (to illustrate this, see the example in Fig. A for A1), with i = 1, 2, 3), namely $Ri_{mean}$. Then, the total mean of $R_d$ is computed over the $Ai_{lat}$ and $Ai_{lon}$ rectangles (see Fig. A1) associated to each Ai, namely $Ri_{lat}$ and $Ri_{lon}$. $Ri_{lat}$ and $Ri_{lon}$ are, as expected, less than $Ri_{mean}$. The selected limits of $Ai_{lat}$ and $Ai_{lon}$ contain Ai and are arbitrarily specified, on the basis of the observed *R* distribution. To perform this, we took into account the systematically observed deep decrease and steep increase of precipitation over the W-E and N-S boundaries, in $Ai_{lat}$ and $Ai_{lon}$ respectively, due to the SALLJ effect and the income of humidity.

With the definition of $Ri_{mean} - Ri_{lat} = diff_{lat}(Ri)$ and $Ri_{mean} - Ri_{lon} = diff_{lon}(Ri)$ (both of them positive values), the events belonging to Mi are selected only for those *k* days that verify $Ri_{mean}(k) - Ri_{lat}(k) > diff_{lat}(Ri)$ and $Ri_{mean}(k) - Ri_{lon}(k) > diff_{lon}(Ri)$. $Ri_{mean}(k)$, $Ri_{lat}(k)$ and $Ri_{lon}(k)$ specify that the *R* averages are computed over a single *k* day.

**Fig. A**. $A1_{lat}$ (horizontally shaded) and $A1_{lon}$ (vertically shaded), both including subregion A1 (see text), which corresponds to the northern hotspot of precipitation found.

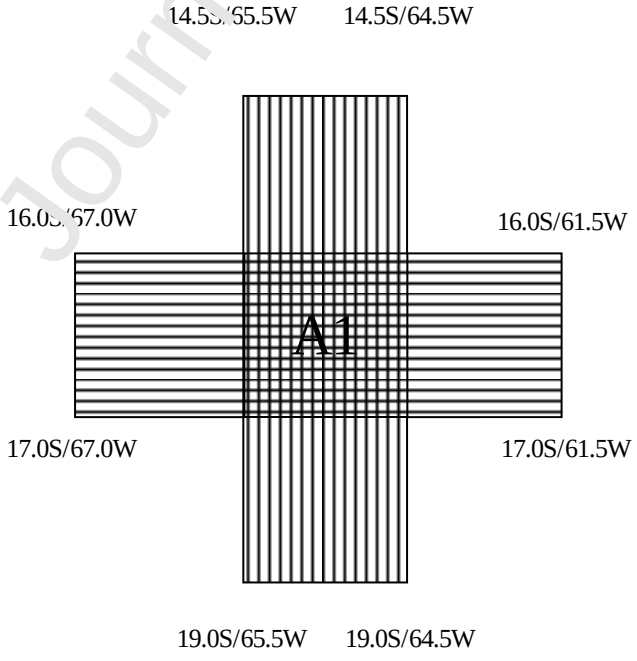

Author Statement

Hierro R., designed the study, performed the analysis, created the figures and wrote the draft of the paper.

Maryam Ramezani Ziarani contributed in conceptualization, methodology, data preparation and review and editing.

Burgos Fonseca, contribuited with the data preparation.

M., Llamedo, P, Schmidt, T., de la Torre, A., Alexander, P. contributed to discussing the results and finalizing the manuscript.

No conflict of interest

**References**

Banta, R.M., 1990. The role of mountain flows in making clouds. In: Atmospheric processes over Complex Terrain. Meteorol. Monographs 23, 229-283.

Barros, A.P. and T.J. Lang, 2003. Monitoring the Monsoon in the Himalayas: observations in Central Nepal, June 2001. Mon. Wea. Rev., 131, 1408–1427, https://doi.org/10.1175/1520-0493(2003)131

Boers, N., Rheinwalt, A., Bookhagen, B., Barbosa, H., M., J., Marwan, N., Marengo, J., Kurths, J., 2014. The South American rainfall dipole: A complex network analysis of extreme events, Geophys. Res. Lett., 41, 7397–7405, doi:10.1002/2014GL061829.

Boers, N., Bookhagen, B., Marengo, J., Marwan, N., von Storch, J., Kurths, J., 2015. Extreme Rainfall of the South American Monsoon System: A Dataset Comparison Using Complex Networks. J. Climate, 28, 1031–1056, https://doi.org/10.1175/JCLI-D-14-00340.1

Bookhagen, B., Strecker, M. R., 2008. Orographic barriers, high-resolution TRMM rainfall, and relief variations along the eastern Andes, Geophys. Res. Lett., 35, L06403, doi:10.1029/2007GL032011.

Bookhagen, B., Strecker, M., R., 2012. Spatiotemporal trends in erosion rates across a pronounced rainfall gradient: Examples from the southern Central Andes, Earth Planet. Sci. Lett., 327-328, 97–110, doi:10.1016/j.epsl.2012.02.005.

Cattell R. B., 1952. Factor analysis : an introduction and manual for the psychologist and social scientist. Harper and Row, New York

Chavez, S. P., Takahashi, K., 2017. Orographic rainfall hot spots in the Andes-Amazon transition according to the TRMM precipitation radar and in situ data, J. Geophys. Res. Atmos., 122, 5870–5882, doi:10.1002/2016JD026282.

Compagnucci, R. H., Salles, M. A., Canziani, P. O., 2001. The spatial and temporal behaviour of the lower stratospheric temperature over the Southern Hemisphere: the MSU view. Part I: data, methodology and temporal behaviour. Int. J. Climatol., 21: 419-437. doi:10.1002/joc.606

Compagnucci, R. H. and Richman, M. B., 2008. Can principal component analysis provide atmospheric circulation or teleconnection patterns?. Int. J. Climatol., 28: 703-726. doi:10.1002/joc.1574

de la Torre, A., Daniel, V., Taillea[illegible] K. and Teitelbaum, H., 2004. A deep convection event above the Tunuyán Valley near to the Andes Mountains. Mon. Weather Rev. 132 (9), 2259–2268.

Fernández, J. P. R., Franchito, S., H., Rao, B., V., 2006. Simulation of the summer circulation over South America by two regional climate models. Part I: Mean climatology. Theor. Appl. Climatol., 86, 247-260.

Fonseca I., Cavalcanti, A., 2012. Large scale and synoptic features associated with extreme precipitation over South America: A review and case studies for the first decade of the 21st century. Atmos. Res., 118, 27-40, ISSN 0169-8095, https://doi.org/10.1016/j.atmosres.2012.06.012.

Gulizia, C., Camilloni, I., Doyle, M., 2013. Identification of the principal patterns of summer moisture transport in South America and their representation by WCRP/CMIP3 global climate models. Theor. Appl. Climatol., 112, 227–241. doi: 10.1007/s00704-012-0729-4

Harden, C. P., 2006. Human Impacts on Headwater Flu- vial Systems in the Northern and Central Andes. Geo- morphology 79 (3-4): 249-263.

Hierro, R. , Llamedo, P. , de la Torre, A. and Alexander, P., 2016. Spatiotemporal structures of rainfall over the Amazon basin derived from TRMM data. Int. J. Climatol., 36: 1565-1574. doi:10.1002/joc.4429

Hobouchian, M.P., P. Salio, Y. García Skabar, D. Vila, 2017. Garreaud, R. Assessment of satellite precipitation estimates over the slopes of the subtropical andes. Atmos. Res. 2017, 190, 43–54.

Hoffman, J., 1975. Maps of mean temperature and precipitation in Climatic Atlas of South America, vol. 1, pp. 1–28, World Meteorol. Org. Geneva, Switzerland.

Horel, J. D., Hahmann, A., N., Geisler, J. E., 1989. An investigation of the annual cycle of convective activity over the tropical Americas. J. Climate, 2, 1388-1403.

Huffman, G.J., D.T. Bolvin, E.J. Nelkin, D.B. Wolff, R.F. Adler, G. Gu, Y. Hong, K.P. Bowman, and E.F. Stocker, 2007. The TRMM Multisatellite Precipitation Analysis (TMPA): Quasi-Global, Multiyear, Combined-Sensor Precipitation Estimates at Fine Scales. J. Hydrometeor., 8, 38–55, https://doi.org/10.1175/JHM560.1

Iribarne, J. V., Godson, W., L., 1973. *Atmospheric Thermodynamics*. D. Reidel, 222 pp.

Jamandre, C. A., Narisma, G. T., 2013. Spatio-temporal validation of satellite-based rainfall estimates in the Philippines, Atmos. Res., 122, 599-608, ISSN 0169-8095, https://doi.org/10.1016/j.atmosres.2012.06.024.

Kousky, V. E., 1988. Pentad outgoing longwave radiation climatology for the South American sector. Rev. Bras. Meteorol., 3, 217-231.

Kumar S., Y. Silva, A. Moya, D. Martínez, 2019. Effect of the surface wind flow and topography on precipitating cloud systems over the Andes and associated Amazon basin: GPM observations. Atmos. Res., 225:193-208. doi: https://doi.org/10.1016/j.atmosres.2019.03.027

Kummerow, C., J. Simpson, O. Thiele, W. Barnes, A.T. Chang, E. Stocker, R.F. Adler, A. Hou, R. Kakar, F. Wentz, P. Ashcroft, T. Kozu, Y. Hong, K. Okamoto, T. Iguchi, H.

Kuroiwa, E. Im, Z. Haddad, G. Huffman, B. Ferrier, W.S. Olson, E. Zipser, E.A. Smith, T.T. Wilheit, G. North, T. Krishnamurti, and K. Nakamura, 2000. The Status of the Tropical Rainfall Measuring Mission (TRMM) after Two Years in Orbit. J. Appl. Meteor., 39, 1965–1982, https://doi.org/10.1175/1520-0450(2001)040<1965:TSOTTR>2.0.CO;2

Liebmann, B., Marengo, J. A., 2001. Interannual variability of the rainy season and rainfall in the Brazilian Amazon Basin. J. Climate, 14, 4308-4318.

Lowman, L. E., Barros, A., P., 2014. Investigating links between climate and orography in the central Andes: Coupling erosion and precipitation using a physical-statistical model, J. Geophys. Res. Earth Surf., 119, 1322–1353, doi:10.1002/2013JF002940.

Mantas, V.M., Liu, Z., Caro, C., Pereira, A.J.S.C., 2015. Validation of TRMM multi-satellite precipitation analysis (TMPA) products in the Peruvian Andes, Atmos. Res., 163, 132-145, https://doi.org/10.1016/j.atmosres.2014.11.012.

Marengo, J. A., B. Liebmann, V. E. Kousky, N. P. Filizola, and I. C. Wainer, 2001: Onset and end of the rainy season in the Brazilian Amazon Basin. J. Climate, 14, 833-852.

Marengo, J. A., Tomasella, J., Soares, W., R., Alves, L., M., Nobre, C., A., 2012a. Extreme climatic events in the Amazon basin: Climatological and hydrological context of recent floods. Theor. Appl. Climatol., 107, 73–85, doi:10.1007/s00704-011-0465-1.

Montero-López, C., Strecker, M.R., Schildgen, T.F., Hongn, F., Guzmán, S., Bookhagen, B., Sudo, M., 2014. Local high relief at the southern margin of the Andean plateau by 9 Ma: evidence from ignimbritic valley fills and river incision: Terra Nova, v. 26, p. 454–460, doi:10.1111/ter.12120

Moreiras, S. M., 2005. Climatic effect of ENSO associated with landslide occurrence in the central Andes, Mendoza Province, Argentina. Landslides, 2, 53–59, doi:https://doi.org/10.1007/s10346-005-0046-4.

Paegle, J., Zhang, C., D., Baumhefner, D., B., 1987. Atmospheric response to tropical thermal forcing in real data integrations. Mon. Wea. Rev., 115, 2975–2995.

Rasmussen K. L., Houze R. A. Jr., 2011. Orogenic convection in South America as seen by the TRMM satellite, Mon. Weather Rev., 139, 2399–2420.

Rivera, J.A., G. Marianetti, S. Hinrichs, 2018. Validation of CHIRPS precipitation dataset along the Central Andes of Argentina. Atmos. Res., 213, 437–449.

Romatschke U., Houze R. A. Jr., 2013. Characteristics of precipitating convective systems accounting for the summer rainfall of tropical and subtropical South America, J. Hydrometeorol., 14, 25–46.

Rozante, J. R., Cavalcanti, F., A., 2008. Regional Eta model experiments: SALLJEX and MCS development, J. Geophys. Res., 113, D17106, doi:10.1029/2007JD009566.

Saavedra, M., C. Junquas, J.C. Espinoza, Y. Silva, 2019. Impacts of topography and land use changes on the air surface temperature and precipitation over the central Peruvian Andes, Atmos. Res., 104711, ISSN 0169-8095, https://doi.org/10.1016/j.atmosres.2019.104711.

Seluchi, M. E., Marengo, J., A., 2000. Tropical-midlatitude exchange of air masses during DJF and JJA in South America: Climatic aspects and examples of intense events, Int. J. Climatol., 20, 1167–1190.

Trachte, K., Rollenbeck, R., Bendix, J., 2010. Nocturnal convective cloud formation under clear-sky conditions at the eastern Andes of south Ecuador, J. Geophys. Res., 115, D24203, doi:10.1029/2010JD014140.

Vera, C., J. Baez, M. Douglas, C.B. Emmanuel, J. Marengo, J. Meitin, M. Nicolini, J. Nogues-Paegle, J. Paegle, C. Penalba, P. Salio, C. Saulo, M.A. Silva Dias, P. Silva Dias, and E. Zipser, 2006 (a). The South American Low-Level Jet Experiment. Bull. Amer. Meteor. Soc., 87, 63–77, https://doi.org/10.1175/BAMS-87-1-63.

Vera, C., W. Higgins, J. Amador, T. Ambrizzi, R. Garreaud, D. Gochis, D. Gutzler, D. Lettenmaier, J. Marengo, C.R. Mechoso, J. Nogues-Paegle, P.L. Dias, and C. Zhang, 2006 (b). Toward a Unified View of the American Monsoon Systems. J. Climate, 19, 4977–5000, https://doi.org/10.1175/JCLI3896.1

Virji, H., 1981. A preliminary study of summertime tropospheric circulation patterns over South America estimated from cloud winds. Mon. Wea. Rev., 109, 599–610.

Wang H, Fu R., 2002. Cross-equatorial flow and seasonal cycle of precipitation over South America. J Clim 15:1591–1608

Whipple, K.X. The influence of climate on the tectonic evolution of mountain belts. Nature Geosci., 2, 204 97-104 (2009).

Highlights

- Three strong rainfall signals appear in the mean accumulated rainfall in the eastern central Andes.
- Daily statistics indicate that the extreme events detected are produced during the night.
- This rainfall distribution might be explained by cooling downslope air converging at the surface with low-level unstable layers and/or a forced lifting created by the mountains.